Phase-field modeling of microstructural pattern formation during directional solidification of peritectic alloys without morphological instability

Tak Shing Lo,[1,2] Alain Karma,[1] and Mathis Plapp[1,3]
[1]*Physics Department and Center for Interdisciplinary Research on Complex Systems, Northeastern University, Boston, Massachusetts 02115*
[2]*Courant Institute of Mathematical Sciences, New York University, New York, New York 10012*
[3]*Laboratoire de Physique de la Matière Condensée, CNRS/Ecole Polytechnique, 91128 Palaiseau, France*
(Received 29 May 2000; published 27 February 2001)

During the directional solidification of peritectic alloys, two stable solid phases (parent and peritectic) grow competitively into a metastable liquid phase of larger impurity content than either solid phase. When the parent or both solid phases are morphologically unstable, i.e., for a small temperature gradient/growth rate ratio (G/v_p), one solid phase usually outgrows and covers the other phase, leading to a cellular-dendritic array structure closely analogous to the one formed during monophase solidification of a dilute binary alloy. In contrast, when G/v_p is large enough for both phases to be morphologically stable, the formation of the microstructure becomes controlled by a subtle interplay between the nucleation and growth of the two solid phases. The structures that have been observed in this regime (in small samples where convection effects are suppressed) include alternate layers (bands) of the parent and peritectic phases perpendicular to the growth direction, which are formed by alternate nucleation and lateral spreading of one phase onto the other as proposed in a recent model [R. Trivedi, Metall. Mater. Trans. A **26**, 1 (1995)], as well as partially filled bands (islands), where the peritectic phase does not fully cover the parent phase which grows continuously. We develop a phase-field model of peritectic solidification that incorporates nucleation processes in order to explore the formation of these structures. Simulations of this model shed light on the morphology transition from islands to bands, the dynamics of spreading of the peritectic phase on the parent phase following nucleation, which turns out to be characterized by a remarkably constant acceleration, and the types of growth morphology that one might expect to observe in large samples under purely diffusive growth conditions.

DOI: 10.1103/PhysRevE.63.031504 PACS number(s): 64.70.Dv, 81.30.Fb, 05.70.Ln

I. INTRODUCTION

The spontaneous emergence of complex microstructural patterns during the solidification of alloys is a subject of both fundamental and applied interest [1]. During directional solidification, a sample is pulled in an externally imposed temperature gradient G with a fixed pulling speed v_p. This setup has been used extensively in fundamental studies of solidification patterns because it allows one to study their formation under well-controlled growth conditions. Depending on the type of alloy and the ratio G/v_p, various patterns are possible. During monophase solidification of a dilute binary alloy, solute redistribution leads to a well-known morphological instability (Mullins-Sekerka instability [2]) below a critical ratio G/v_p, and cellular or dendritic patterns are typically formed. For nondilute alloy concentrations close to a eutectic point, two stable solid phases of different compositions can grow from a metastable liquid. In this case, the two phases cooperate and form lamellae or rods parallel to the growth direction (coupled growth). For off-eutectic compositions, coexistence between dendrites and coupled growth structures is also observed.

Much less is known about microstructural pattern formation in peritectic growth [1], despite the fact that many industrially important metallic alloy systems as well as ceramics such as the high-T_c superconductor YBCO are peritectics. A schematic phase diagram of a peritectic AB alloy (where B will be called the impurity for convenience) is shown in Fig. 1. It contains a peritectic point, analogous to the eutectic point, at which two different solid phases, the parent (primary or α) and peritectic (secondary or β) phases, coexist with a liquid of higher composition than either solid

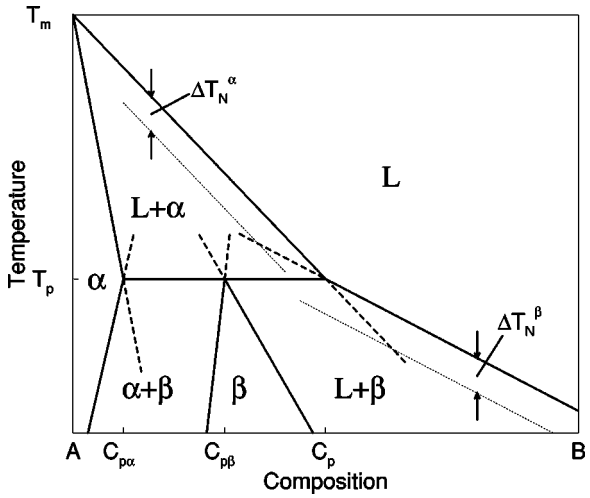

FIG. 1. Schematic phase diagram of a peritectic alloy. C, concentration of impurity B; T_m, melting point of pure A; T_p, peritectic temperature. C_p, $C_{p\beta}$, and $C_{p\alpha}$ are the compositions of the liquid, β solid, and α solid that are in equilibrium at T_p. ΔT_N^α and ΔT_N^β are the nucleation undercoolings for α and β phases, respectively. Dashed lines are metastable extensions of the liquidus and solidus lines.

phase. Above the peritectic temperature T_p, the parent phase is stable and the peritectic phase is metastable, whereas below T_p, the opposite is true. For comparison, in a eutectic, both solid phases are stable below the eutectic temperature, and metastable above, and the impurity concentration in the liquid falls in between the concentrations of the two solid phases. For a sufficiently low G/v_p ratio, a dendritic array structure of the parent *or* the peritectic phase is typically observed, and which of these two phases is selected depends on the alloy composition and G/v_p [3]. In contrast, for a high G/v_p ratio morphological instability is suppressed. In this case, banded structures made up of alternating layers of primary and peritectic phases perpendicular to the growth direction are formed. These structures have by now been observed in various peritectic systems, including Sn-Cd [4,5], Sn-Sb [6], Zn-Cu [6], Ag-Zn [7], and Pb-Bi [8,9]. It is worth noting that eutecticlike coupled growth structures, which are quite distinct from banded structures, have recently been observed in the Fe-Ni system [10]. Whether stable coupled growth is theoretically possible during peritectic growth has remained an open question for quite some time [4], and we will address this issue elsewhere. Here, we focus primarily on banded structure formation and phenomena associated with the dynamical spreading of one solid phase onto the other.

Recently, Trivedi has introduced a one-dimensional (1D) model [11] to explain the formation of peritectic banded structures for purely diffusion-controlled growth. The conceptual banding cycle assumed in this model is as follows. Consider a melt with homogeneous composition $C_\infty < C_p$ being solidified starting from a flat α-liquid interface in equilibrium. The rejection of impurities B into the liquid during solidification leads to the buildup of a solutal boundary layer. As a result, the interface temperature decreases, following the liquidus curve in the phase diagram. If C_∞ is large enough, the interface temperature eventually falls sufficiently below T_p for the peritectic phase to nucleate heterogeneously at the solid-liquid interface before the growth of the α phase has reached its steady state. The newly nucleated β phase rejects fewer impurities than the α phase. Consequently, the magnitude of the solutal boundary layer decreases and the interface temperature increases, following now the β-liquid coexistence line in the phase diagram. If C_∞ is low enough, such that the corresponding interfacial temperature is sufficiently higher than T_p, the α solid may renucleate again before the steady state is reached, and the cycle repeats. Therefore, this model predicts that bands can form only when the composition falls inside a narrow window in the hypoperitectic region ($C_{p\alpha} < C_\infty < C_{p\beta}$) whose width depends on the nucleation undercoolings ΔT_N^α and ΔT_N^β.

The first attempts to validate this prediction experimentally yielded contradictory results. Directional solidification experiments with Pb-Bi and Sn-Cd alloys seemed to show that bands also form in the hyperperitectic region ($C_{p\beta} < C_\infty < C_p$), in apparent contradiction with this prediction. An attempt was made to resolve this ''composition range paradox'' by incorporating convection effects [12], assuming the existence of a fully mixed liquid of uniform composition outside a purely diffusive 1D boundary layer of finite thickness. This model, however, yielded a banding cycle and band spacings that are inconsistent with experimental results, hinting that this boundary-layer approximation (typically valid for strong convection) is inadequate to describe these experiments. Around the same time, careful serial sectioning of solidified Pb-Bi and Sn-Cd alloys revealed that the seemingly banded structures are actually oscillatory treelike structures connected in three dimensions [13], and not discrete bands, thereby resolving experimentally this composition range paradox. Following this finding, a more accurate model was developed that assumes a planar solidification front, but incorporates a fully two-dimensional convection flow field [14]. This model successfully reproduced the observed oscillatory structures.

Following these studies, experiments were conducted in thin tubes to reduce convection [13]. For tube diameters smaller than 1 mm, truly discrete bands indeed became observable inside a narrow composition range predicted by the 1D diffusive growth model. Surprisingly, however, it was also observed that when the tube diameter was further reduced, ''islands'' of the β phase formed inside the matrix of the α phase, instead of discrete bands. This observation suggests that there is a microstructural transition from bands to islands if the system size is reduced. It was also observed that islands tend to form more easily for initial compositions closer to $C_{p\alpha}$. In addition, some spatially chaotic patterns were observed in some experiments. The formation of these structures is controlled by a subtle interplay between the nucleation process and the competition between the growth of the nuclei and the preexisting phase. In this respect, the one-dimensional model may not always be adequate to describe this competition because it assumes an infinite spreading speed for the newly nucleated phase. Moreover, the 2D convection model assumes a flat interface and is hence not well suited to simulate heterogeneous nucleation and spreading. In order to model accurately the formation of these different structures, a truly 2D model of interface evolution is necessary. The particular difficulty of this problem is that the microstructure formation is controlled by an interplay between nucleation and growth of the different phases. No steady-state growth mode exists, which makes the whole problem explicitly time dependent.

In this paper, we use a phase-field approach [15–22] to investigate the formation of this class of banded microstructures in a purely diffusive regime and a 2D geometry. The phase-field method eliminates the need of explicit front tracking and thus greatly simplifies the task of numerically solving the equations of peritectic solidification that involve three-phase junctions. A phase-field model for peritectic growth has recently been proposed [23]. Here, we use an alternative model that is closer to the eutectic model of Wheeler *et al.* [22].

We first investigate the spreading of the peritectic phase on the primary phase after a single nucleation event. We characterize in detail the dynamics of the three-phase junction during spreading and find a morphological transition from discrete bands of α and β phases to isolated islands of β phase when the system size is decreased, in qualitative agreement with experiments. Moreover, our simulations en-

able us to understand physically the basic mechanism that underlies this transition. We then investigate the effect of multiple nucleations on microstructure formation in large systems by supplementing the phase-field equations with a phenomenological stochastic nucleation law.

The remainder of this article is organized as follows. In Sec. II, we write down the sharp-interface and phase-field models. Section III is devoted to the study of the equilibrium properties of the phase-field model and Sec. IV describes the simulation method. Results are presented in Sec. V, followed by a summary and conclusions in Sec. VI.

II. MODEL

A. Sharp-interface model

The sharp-interface equations are given by

$$\partial_t C = D_L \nabla^2 C, \tag{1}$$

$$v_n (C_L - C_\nu) = -D_L \partial_n C_L, \tag{2}$$

$$T = T_p + m_\nu (C_L - C_p) - \Gamma_\nu K - \frac{1}{\mu_\nu} v_n, \tag{3}$$

where C denotes the concentration of impurity B, and the subscript ν labels the solid α and β phases. Equation (1) is the diffusion equation for the solute in the liquid with the solute diffusivity D_L. We have assumed that diffusion in the solid is negligible (one-sided model). Equation (2) expresses the mass conservation at the moving interface, with v_n and ∂_n denoting the normal velocity of the interface and the derivative normal to the interface, respectively. Finally, Eq. (3) is the Gibbs-Thomson condition at the solid-liquid interface, with K, m_ν, μ_ν and Γ_ν being the interface curvature, liquidus slope, kinetic coefficient, and Gibbs-Thomson constant of phase ν, respectively. The Gibbs-Thomson constants Γ_ν are defined by

$$\Gamma_\nu = \frac{\gamma_{\nu L} T_p}{L_\nu}, \tag{4}$$

where $\gamma_{\nu L}$ is the surface energy of the ν-liquid interface and L_ν is the latent heat of fusion for phase ν, both taken at the peritectic temperature. Young's condition

$$\gamma_{\alpha L} \mathbf{t}_{\alpha L} + \gamma_{\beta L} \mathbf{t}_{\beta L} + \gamma_{\alpha\beta} \mathbf{t}_{\alpha\beta} = \mathbf{0} \tag{5}$$

must be satisfied at the trijunction points where three phases meet, where $\mathbf{t}_{\mu\nu}$ is the unit vector parallel to the μ-ν interface and pointing away from the trijunction.

B. Phase-field model

To distinguish between the three possible phases (liquid, α solid, and β solid), we follow a similar approach to that of Wheeler *et al.* [22] for eutectic solidification by introducing two nonconserved order parameters (phase fields) ϕ and ψ. The first distinguishes between solid ($\phi = 1$) and liquid ($\phi = -1$), the second between the α solid ($\psi = 1$) and the β solid ($\psi = -1$). The solid-liquid interface is defined by the level curve $\phi = 0$, and the interface between the solid α and β phases is defined by the level curve $\psi = 0$ when ϕ is positive. One important difference from Ref. [22] is that in our model ψ takes the well-defined value $\psi = 0$ in the liquid. This modification is necessary because, in the model of Wheeler *et al.*, the equation of motion for ψ becomes a simple diffusion equation in the liquid. This introduces an undesirable new time scale in dynamical simulations that is removed in the present approach.

As a third dynamical variable we need the composition C, which is a conserved field. We define the scaled composition

$$c(\mathbf{r},t) = [C(\mathbf{r},t) - C_{p\beta}] / \Delta C_\alpha, \tag{6}$$

where $\Delta C_\nu = (C_p - C_{p\nu})$, $\nu = \alpha, \beta$, is the concentration jump at the ν-liquid interface at T_p.

In terms of these quantities, the equations of motion that govern the dynamics of the system are given by

$$\tau_\phi \frac{\partial \phi}{\partial t} = -\frac{\delta F}{\delta \phi}, \tag{7}$$

$$\tau_\psi \frac{\partial \psi}{\partial t} = -\frac{\delta F}{\delta \psi}, \tag{8}$$

$$\frac{\partial c}{\partial t} = \boldsymbol{\nabla} \cdot \left[M(\phi) \boldsymbol{\nabla} \frac{\delta F}{\delta c} \right], \tag{9}$$

where F is the dimensionless free energy of the system (i.e., the Helmholtz free energy, divided by the product of the system size and a typical value of the free energy density that sets the physical energy scale), $M(\phi)$ is the mobility of the impurities, and τ_ϕ and τ_ψ are (fast) relaxation times for the phase fields. These equations are of the standard variational form known from out-of-equilibrium thermodynamics. Note that, since $\delta F / \delta c$ is the local chemical potential μ, Eq. (9) is simply the continuity equation for the impurity concentration with the mass current $\mathbf{J}$ given by

$$\mathbf{J} = -M(\phi) \boldsymbol{\nabla} \mu. \tag{10}$$

If there are no fluxes across the boundary of the volume where F is defined, $dF/dt \leqslant 0$ and Eqs. (7)–(9) imply that the dynamics drives the system toward a minimum of free energy.

The free energy functional of the system is assumed to be of the form

$$F = \int \{ \tfrac{1}{2} W_\phi^2 |\boldsymbol{\nabla} \phi|^2 + \tfrac{1}{2} W_\psi^2 |\boldsymbol{\nabla} \psi|^2 + f(\phi, \psi, c) \} d\mathbf{r}. \tag{11}$$

Since F, ϕ, and ψ are dimensionless, the coefficients W_ϕ and W_ψ have the dimension of length: they determine the width of the diffuse interfaces. The form of the free energy density is chosen such that there are two minima at $\psi = \pm 1$ corresponding to the α $(+)$ and β $(-)$ phases for $\phi = +1$. There is a single minimum in the liquid corresponding to $\phi = -1$ and $\psi = 0$, and $f(\phi, \psi, c)$ has a single minimum as a function of c for fixed values of ϕ and ψ corre-

sponding to the three equilibrium phases. A convenient way to match these requirements is to construct a free energy density of the form

$$f(\phi,\psi,c)=\frac{\lambda}{2}\{c+A_1 h(\phi)+\tfrac{1}{2}A_2[1+h(\phi)]h(\psi)\}^2 - \lambda\{B_1 h(\phi)+\tfrac{1}{2}B_2[1+h(\phi)]h(\psi)\}+g(\phi) + \tfrac{1}{2}[1+h(\phi)]g(\psi)+\tfrac{1}{2}[1-h(\phi)]\psi^2. \quad (12)$$

Here, λ is a positive constant, and A_1, A_2, B_1, and B_2 are functions of temperature. The function g is a double-well potential with minima at ± 1, and the function h must satisfy $h(\pm 1)=\pm 1$ and $h'(\pm 1)=0$ in order to keep the minima of f at constant values of ϕ and ψ, independent of the value of c. We take

$$g(\phi)=1/4-\phi^2/2+\phi^4/4, \quad (13)$$

$$h(\phi)=3(\phi-\phi^3/3)/2. \quad (14)$$

The functions $g(\psi)$ and $h(\psi)$ are similarly defined. It follows trivially from Eq. (12) that the bulk phase free energy densities are given by

$$f_L \equiv f(-1,0,c)=\frac{\lambda}{2}(c-A_1)^2+\lambda B_1, \quad (15)$$

$$f_\alpha \equiv f(1,1,c)=\frac{\lambda}{2}(c+A_1+A_2)^2-\lambda(B_1+B_2), \quad (16)$$

$$f_\beta \equiv f(1,-1,c)=\frac{\lambda}{2}(c+A_1-A_2)^2-\lambda(B_1-B_2). \quad (17)$$

For the mobility function $M(\phi)$, we take

$$M(\phi)=\frac{D_L}{2\lambda}(1-\phi). \quad (18)$$

With this choice, the diffusion coefficient of the impurity is a constant equal to D_L in the liquid and zero in both solids, which corresponds to the so-called one-sided model. A standard asymptotic analysis of the sharp-interface limit of the present phase-field model [24] shows that Eqs. (7)–(9) reduce as expected to Eqs. (1)–(3). The relation between the parameters in the two sets of equations is given in the next section.

III. PHASE DIAGRAM AND EQUILIBRIUM PROPERTIES

By applying the well-known common tangent construction to the bulk free energy densities given by Eqs. (15)–(17), we can construct the equilibrium phase diagram of the phase-field model. The equilibrium compositions can be expressed in terms of the temperature-dependent functions A_1, A_2, B_1, and B_2 (see the Appendix). However, since there are only four functions, we can at most fit four lines out of six in the phase diagram (i.e., three pairs corresponding to α-liquid, β-liquid, and α-β coexistence). We may choose to construct, say, the two liquidus lines and the two solidus lines and leave the two solid-solid coexistence curves determined by Eq. (A3) and Eq. (A4). Since we are interested only in the behavior of the system at temperatures close to T_p, we assume for simplicity that the liquidus and solidus lines are straight, and that the concentration jumps at the solid-liquid interface are constant (liquidus and solidus are parallel). We can then choose A_1 and A_2 as constants and B_1 and B_2 as linear functions of the temperature. The corresponding expressions for the functions A_1, A_2, B_1, and B_2 are given in the Appendix expressed in terms of the dimensionless temperature field

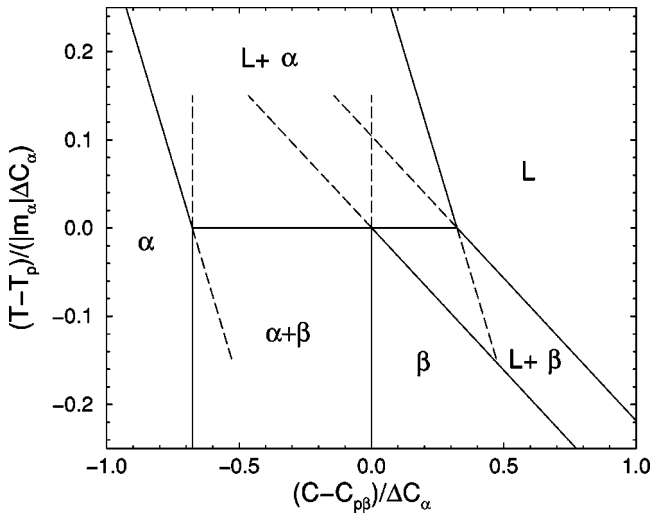

FIG. 2. Phase diagram for our model system. Dashed lines are metastable extensions of the liquidus and solidus lines.

$$\tilde{T}=\frac{(T-T_p)}{|m_\alpha|\Delta C_\alpha}, \quad (19)$$

which is a measure of the temperature relative to T_p normalized by the freezing range of the α phase.

In the present model, there exists a temperature-dependent concentration c_u such that, in the solid, the solid α (β) phase is thermodynamically stable only if $c<c_u$ ($c>c_u$). By comparing Eq. (16) and Eq. (17), it is easy to show that c_u is exactly midway between the two solid-solid coexistence lines. In order to avoid a phase transformation in the solid far behind the solid-liquid interface, we require c_u to be independent of temperature. One way to achieve this is to make the solid-solid coexistence lines vertical by choosing suitable parameters. This difference from a real peritectic phase diagram is unlikely to change the qualitative behavior of the system. A phase diagram for the model system used in our simulations is shown in Fig. 2.

The equilibrium interface profiles connecting different phases can be obtained by solving the time-independent one-dimensional version of the equations of motion with suitable boundary conditions. Since the chemical potential must be constant at equilibrium, the relation

$$\mu=\frac{\delta F}{\delta c}=\frac{\partial f}{\partial c} \quad (20)$$

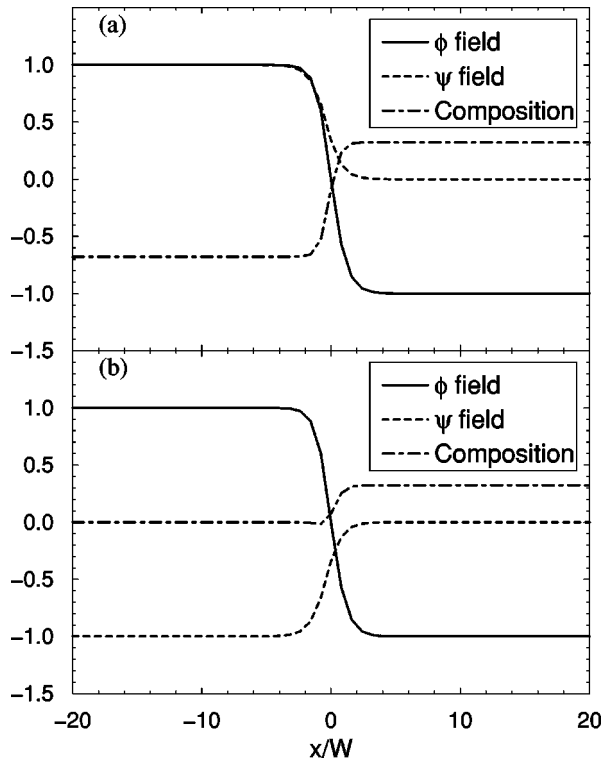

FIG. 3. Equilibrium profiles for (a) α-L equilibrium and (b) β-L equilibrium at T_p ($\lambda=2.5$). The composition is scaled according to Eq. (6).

can be used to eliminate the concentration field from Eqs. (7) and (8). The appropriate value of μ for a certain temperature is obtained from the common tangent construction. The two resulting coupled ordinary differential equations were solved numerically using a Newton-Raphson method on a one-dimensional grid of spacing Δx. For simplicity, we assumed $W_\phi = W_\psi = W$. Unless otherwise stated, all the results below are obtained for $\Delta x/W = 0.8$, which provides a good compromise between computational efficiency and accuracy. The resulting equilibrium profiles, centered at the origin, for the phase fields and the concentration for α-L equilibrium and β-L equilibrium at T_p are shown in Fig. 3. For solid-solid equilibrium, the interface profile of ψ can be obtained analytically because $\phi = +1$ is a constant:

$$\psi_0(x) = -\tanh\left(\frac{x}{\sqrt{2}W}\right). \tag{21}$$

In all cases, the concentration profiles are given by substituting the equilibrium profiles $\phi_0(x)$ and $\psi_0(x)$ obtained previously into Eq. (20).

With the equilibrium interface profiles at hand, we can calculate the surface energies $\gamma_{\alpha L}$, $\gamma_{\beta L}$, and $\gamma_{\alpha\beta}$, defined as the excess Gibbs free energy per unit surface area. They are given by the expressions

$$\gamma_{\mu\nu} = \int_{-\infty}^{\infty} [W_\phi^2(\partial_x\phi_0)^2 + W_\psi^2(\partial_x\psi_0)^2]dx, \tag{22}$$

where ϕ_0 and ψ_0 are the equilibrium profiles of the phase fields connecting phases μ and ν. The same formula for the surface energies can also be obtained by a matched asymptotic expansion [24]. For the solid-liquid interfaces, the surface energies are obtained by numerical integration. For this purpose, it is more convenient to convert Eq. (22) to a form without the gradients of the fields. Making use of the steady-state one-dimensional version of the equations of motion and the fact that μ is constant in equilibrium, we obtain after some algebra

$$\frac{d}{dx}\left[\frac{1}{2}[W_\phi^2(\partial_x\phi_0)^2 + W_\psi^2(\partial_x\psi_0)^2]\right] = \frac{d}{dx}(f-\mu c). \tag{23}$$

Now one can integrate Eq. (23) from $-\infty$ to an arbitrary x and make use of the expression for the equilibrium concentration profile and the bulk phase values to show that for the solid-liquid interfaces

$$\begin{aligned}\frac{1}{2}[W_\phi^2(\partial_x\phi_0)^2 + W_\psi^2(\partial_x\psi_0)^2] &= g(\phi_0) + \frac{1}{2}[1+h(\phi_0)]g(\psi_0) + \frac{1}{2}[1-h(\phi_0)]\psi_0^2 \\ &\quad + \frac{\lambda}{2}\left(\frac{\overline{B}}{\overline{A}} - B_2\right)[1+h(\phi_0)][h(\psi_0)\mp 1].\end{aligned} \tag{24}$$

Here the upper and lower signs are for α-liquid and β-liquid equilibrium, respectively, and $\overline{A}$ and $\overline{B}$ are defined in the Appendix. For the solid-solid interface, the surface energy $\gamma_{\alpha\beta}$ can be calculated exactly and is equal to $2\sqrt{2}W_\psi/3$.

Related to the surface energies are the two capillary lengths d_0^α and d_0^β defined as

$$d_0^\nu = \frac{\gamma_{\nu L}}{(\Delta c_\nu)^2(\partial\mu/\partial c)}, \tag{25}$$

which can also be expressed in terms of the Gibbs-Thomson constants Γ_ν by

$$d_0^\nu = \frac{\Gamma_\nu}{|m_\nu|\Delta C_\nu}. \tag{26}$$

These are two of the physical length scales that are relevant in pattern formation in solidification problems. In real systems, the capillary lengths are microscopic and much smaller than all other physical length scales in the problem. Ideally, one would like to adjust the capillary lengths in the model to match the physical length scale ratios by choosing suitable model parameters. Since $\partial\mu/\partial c = \lambda$, it follows that d_0^ν depends on λ as

$$d_0^\nu \propto \frac{\gamma_{\nu L}}{\lambda}. \tag{27}$$

Hence, to have small capillary lengths, one would like to increase λ. However, λ cannot be chosen arbitrarily large for two reasons. First, the surface tensions themselves depend

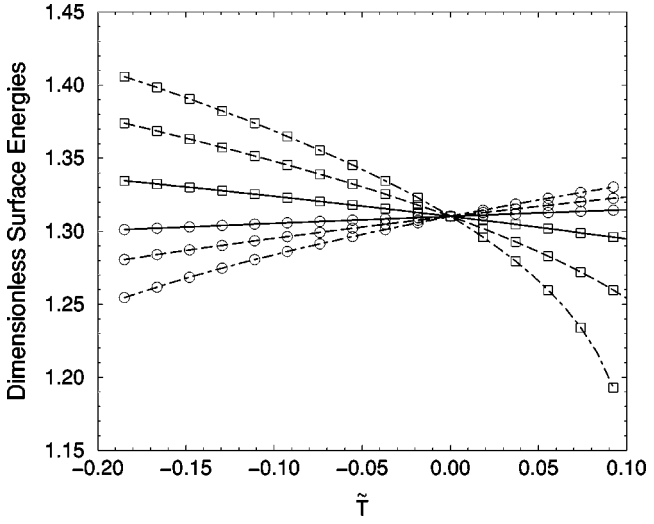

FIG. 4. Dimensionless solid-liquid surface energies versus temperature for different λ. Circles, $\gamma_{\alpha L}/W$; squares, $\gamma_{\beta L}/W$. Solid lines, $\lambda=0.5$; dashed lines, $\lambda=1.5$; and dash-dotted lines, $\lambda=2.5$.

weakly on λ for $T\neq T_p$. As shown in Fig. 4, these variations amount to a few percent over the temperature range of interest when λ is varied by a factor of 5. Secondly, the temperature range in which equilibrium interface solutions exist also depends on λ. More precisely, with a fixed value for λ, the α-liquid equilibrium solution does not exist if T is below a certain value, and the β-liquid interface solution ceases to exist if T is above another value, because if T is too low or too high, the free energy density loses a minimum at ψ equal to $+1$ or -1, respectively. We have estimated the range of temperatures in which both solutions exist for different λ by finding equilibrium solutions at different temperatures. The results are shown in Fig. 5. We can see that this temperature range becomes narrower when λ increases. From now on, we

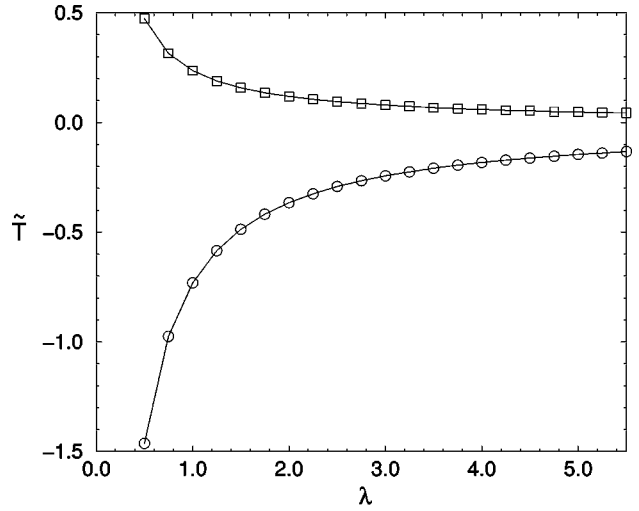

FIG. 5. Temperature range within which both α-liquid and β-liquid equilibrium solutions exist, versus λ. (Circles: limit of existence for α-liquid interface solution. Squares: limit of existence for β-liquid solution.)

fix $\lambda=2.5$ unless otherwise stated. This is a compromise between having a large λ and a sufficient working temperature range in which our two-dimensional simulations can be carried out.

To check Young's condition, we performed two-dimensional simulations at T_p on a square grid with $\Delta x/W=0.8$. The equilibrium angles around a trijunction were measured and found to be consistent with Eq. (5) to within a few degrees. For a moving interface, there are also nonequilibrium kinetic effects related to the attachment of atoms at the interface and solute trapping. Since we are mostly interested here in qualitative aspects of the growth morphologies, we have not analyzed all these effects in detail. We checked, however, by performing dynamical one-dimensional simulations that nonequilibrium effects only lead to a deviation from local equilibrium that does not exceed the Gibbs-Thomson effect caused by interface curvature in two-dimensional simulations.

IV. SIMULATIONS

For our simulations, we cast the equations of motion into a dimensionless form. For simplicity, we take $W_\phi=W_\psi=W$ and $\tau_\phi=\tau_\psi=\tau$. By defining the dimensionless variables

$$\tilde{\mathbf{r}}=\frac{\mathbf{r}}{W},\quad \tilde{t}=\frac{t}{\tau} \tag{28}$$

and the new variable

$$\tilde{\mu}=c+A_1 h(\phi)+\frac{1}{2}A_2[1+h(\phi)]h(\psi), \tag{29}$$

the equations of motion can be written in the form

$$\frac{\partial\phi}{\partial\tilde{t}}=\tilde{\nabla}^2\phi-\frac{\partial f}{\partial\phi}, \tag{30}$$

$$\frac{\partial\psi}{\partial\tilde{t}}=\tilde{\nabla}^2\psi-\frac{\partial f}{\partial\psi}, \tag{31}$$

$$\frac{\partial c}{\partial\tilde{t}}=\alpha\tilde{\nabla}\cdot[\tilde{D}(\phi)\tilde{\nabla}\tilde{\mu}], \tag{32}$$

where

$$\alpha=\frac{\tau D_L}{W^2} \tag{33}$$

is the scaled diffusion coefficient of the impurity in the liquid, and

$$\tilde{D}(\phi)=(1-\phi)/2. \tag{34}$$

Instead of the concentration far from the interface, we may also use η_β, the volume fraction of β formed in the solid, to characterize the overall composition of the sample. The two quantities are related by

$$C_\infty = (1-\eta_\beta)C_{p\alpha} + \eta_\beta C_{p\beta}. \tag{35}$$

In a typical directional solidification experiment, the sample is pulled under a temperature gradient G with a pulling velocity v_p. We define the dimensionless temperature gradient and velocity, $\tilde{G}$ and $\tilde{v}$, by

$$\tilde{G} = \frac{G}{|m_\alpha|\Delta C_\alpha} W, \tag{36}$$

$$\tilde{v}_p = v_p \tau / W. \tag{37}$$

Usually, thermal diffusion is orders of magnitude faster than the diffusion of the impurities, and hence we use the ''frozen temperature approximation'' which assumes that the temperature of the system adjusts instantaneously to the externally imposed temperature gradient. Accordingly, directional growth along the x axis is implemented by letting

$$\tilde{T} = \tilde{T}_0 + \tilde{G}(\tilde{x} - \tilde{v}_p \tilde{t}), \tag{38}$$

where $\tilde{T}_0$ is some reference temperature.

There are five different physical length scales that control the microstructural pattern formation: the two capillary lengths d_0^α and d_0^β defined by Eq. (25), the two thermal lengths

$$l_T^\nu = \frac{|m_\nu|\Delta C_\nu}{G} = \frac{|m_\nu|\Delta C_\nu}{|m_\alpha|\Delta C_\alpha}\frac{W}{\tilde{G}}, \tag{39}$$

and the diffusion length

$$l_D = \frac{D_L}{v_p} = \frac{\alpha}{\tilde{v}_p} W. \tag{40}$$

Equations (30)-(32) are integrated numerically on a two-dimensional grid. We use $\alpha = 1$, $\Delta\tilde{x} = 0.8$, and $\Delta\tilde{t} = 0.1$. Zero-flux boundary conditions are applied to the two sides that are parallel to the growth direction. There are several features in the model that can be exploited in order to speed up the computation. First, the phase fields ϕ and ψ differ significantly from ± 1 only in the interfacial region, and hence we can avoid integrating Eqs. (30) and (31) away from the interface. In addition, Eq. (32) needs to be integrated only in the liquid. Secondly, the concentration field decays exponentially in the growth direction and varies only slowly in space in the liquid region far ahead of the interface. Hence, we can use a coarser and coarser grid as we move away from the interfacial region. Thirdly, in order to simulate a semi-infinite system in the growth direction, we take advantage of the fact that all the fields remain unchanged in the solid in the one-sided model. Whenever the solid-liquid interface has advanced one lattice spacing, we pull the system back by one unit and keep the composition at the end of the liquid side at c_∞. With all these implementations, we are able to carry out simulations with typical lengths in the growth direction equal to about ten times the diffusion length. For the results presented in this article, we chose a pulling speed such as to have a diffusion length of $l_D = 200W$. Other parameters and length scales are listed in Table I.

TABLE I. List of simulation parameters.

λ	2.5	l_T^α/l_D	0.895
$\tilde{G}$	5.5838×10^{-3}	l_T^β/l_D	0.0934
$\tilde{v}_p$	5×10^{-3}	d_0^α/l_D	2.620×10^{-3}
		d_0^β/l_D	2.5119×10^{-2}

V. RESULTS

A. Dynamics of spreading

Let us first concentrate on the spreading of the β phase on the α phase, starting from a single nucleus. Similarly to the situation considered in Trivedi's model, the simulation is started with a homogeneous composition in the liquid and a planar α-liquid interface. The lateral system size L is several times the diffusion length. Nucleations are assumed to occur heterogeneously at the solid-liquid interface when the temperature of the metastable interface reaches a certain undercooling with respect to the stable solid-liquid equilibrium. The nucleation undercoolings ΔT_N^α (α on β) and ΔT_N^β (β on α), shown in Fig. 1, are assumed to be constant. Accordingly, in our simulations a circular nucleus of β phase is put at the solid-liquid interface on one side of the box when the liquid composition at the interface reaches the threshold for nucleation fixed by the nucleation undercooling ΔT_N^β. The radius of the nucleus is taken to be $6W$, slightly larger than the critical radius for nucleation. Since we are interested here in the deterministic spreading dynamics following a single nucleation event, further nucleation is prohibited. Multiple nucleation events will be treated in Sec. V D.

To characterize the dynamics of spreading, we recorded the position and velocity of the trijunction point. The sideways velocity v_y can be regarded as a measure of the spreading speed of the β phase. Figures 6(a) and 6(b) show plots of v_y/v_p versus time for different nucleation undercoolings and different compositions c_∞, respectively. Time is measured in terms of the diffusion time

$$t_D = \frac{l_D}{v_p} = \frac{D_L}{v_p^2}. \tag{41}$$

Two very different regimes of spreading can be clearly distinguished. Immediately after the nucleation, the spreading velocity is almost independent of the composition, but strongly depends on the nucleation undercooling. The growth of the nucleus is influenced only by its immediate surroundings. On the length scale of the nucleus, which is much smaller than the diffusion length, the impurity concentration can be considered constant and is determined only by

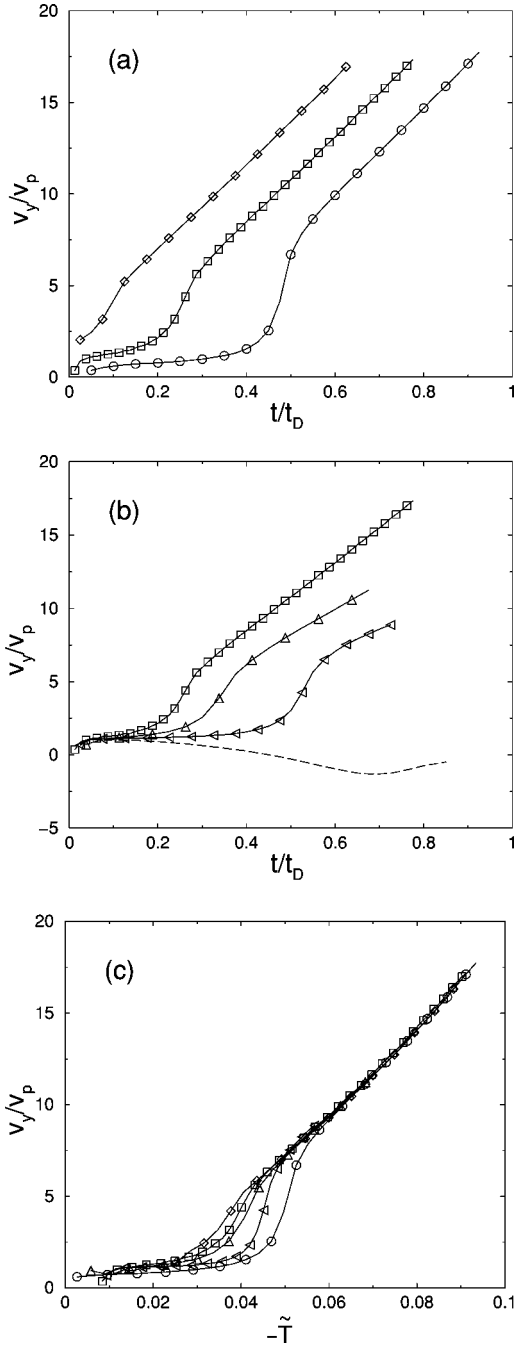

FIG. 6. Plots of v_y/v_p (a) versus time for constant volume fraction and varying nucleation undercooling, (b) versus time for constant nucleation undercooling and varying volume fraction, and (c) versus scaled undercooling $-\tilde{T}$ of the α-L-interface with respect to T_p. Circles, $\eta_\beta=0.375$, $\Delta\tilde{T}_N^\beta=0.018\,78$; squares, $\eta_\beta=0.375$, $\Delta\tilde{T}_N^\beta=0.031\,29$; diamonds, $\eta_\beta=0.375$, $\Delta\tilde{T}_N^\beta=0.043\,81$; upward triangles, $\eta_\beta=0.25$, $\Delta\tilde{T}_N^\beta=0.031\,29$; leftward triangles, $\eta_\beta=0.3125$, $\Delta\tilde{T}_N^\beta=0.031\,29$. The dashed line in (b) is for $\eta_\beta=0.1875$, $\Delta\tilde{T}_N^\beta=0.031\,29$, where an island is formed.

the nucleation undercooling. A higher $\Delta\tilde{T}_N^\beta$ is equivalent to a higher supersaturation, and hence a higher growth speed.

At later times, the modifications of the diffusion field induced by the growing β phase influence the spreading dynamics, and the spreading velocities for equal undercooling but different c_∞ start to differ [Fig. 6(b)]. After a complicated transient, the details of which depend on the choice of parameters, v_y becomes a linear function of time, which means a constant lateral acceleration of the trijunction. This acceleration is independent of the nucleation undercooling or the history of the system, but depends on the composition. An explanation of this finding can be deduced from Fig. 7, which shows the interface temperatures on the sides of the box and at the trijunction as functions of time. After the initial transient, the temperature at the trijunction just follows the temperature on the α side. This implies that the α-liquid interface is almost planar up to the trijunction. We can also see that during the whole time of the simulation the α-liquid interface is still relaxing toward its steady state below T_p. Hence, the undercooling that drives the β phase to spread is increasing.

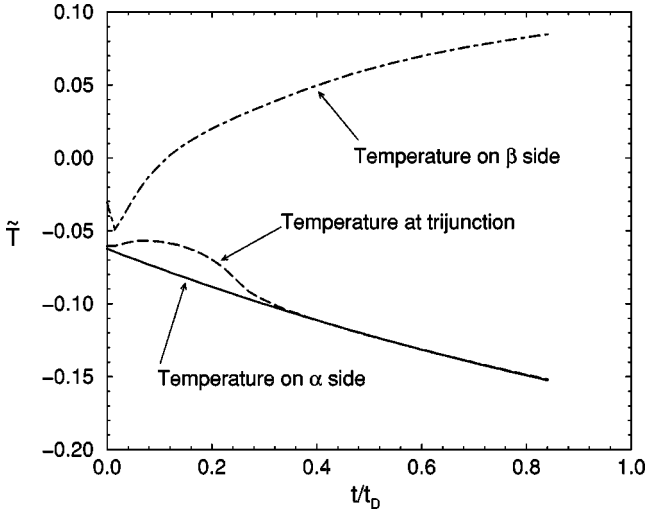

FIG. 7. Scaled temperatures at the trijunction and at the solid-liquid interface on both sides of the box. ($\Delta\tilde{T}_N^\beta=0.031\,29$, $\eta_\beta=0.375$.)

In the late stages of spreading, the lateral diffusion length D/v_y becomes much smaller than the solute boundary layer, and is comparable to or even smaller than the tip of the spreading finger. Therefore, the spreading speed should be a function of local supersaturation only. To check this assumption, we show in Fig. 6(c) the same velocity curves as before, but now plotted against the undercooling of the planar α-liquid interface with respect to the peritectic temperature $-\tilde{T}$. Since in our phase diagram the liquidus curves are straight lines, this undercooling is simply proportional to the supersaturation. The curves all collapse onto a single master curve after the initial transient, i.e., starting from the time when the interface ahead of the trijunction has become flat. This master curve is not linear, and does not smoothly extrapolate to zero. We did not attempt to calculate it theoretically. We expect that its detailed form should depend on the characteristics of the trijunction, and in particular on the angles between the different interfaces. More theoretical and numerical work would be needed to elucidate in detail the role of the various material parameters. Remarkably, similar

observations have been very recently reported in experiments on a transparent organic eutectic alloy [27] during spreading of the secondary phase on a planar interface of primary phase. The spreading speed of the secondary phase showed an approximately linear increase with time, and the data could also reasonably well be rescaled onto an analogous master curve.

Since the α-liquid interface far ahead of the trijunction stays fairly planar before the arrival of the β phase, the time dependence of the temperature on the α side can be well described by the Warren-Langer approximation [25]. The rate of change of the supersaturation is solely determined by the composition c_∞, which explains why the final slope of the curves in Figs. 6(a) and 6(b) depends on c_∞ but not on the nucleation undercooling.

A completely different behavior is observed when the composition is sufficiently low. As shown in Fig. 6(b) (dashed line), the initial spreading speed is the same as for the other runs. However, at later times, the spreading slows down and the trijunction point turns around such that v_y becomes negative. Instead of a band, an isolated island of β phase is formed. This phenomenon will be addressed in detail in Sec. V B below.

In the final regime of spreading, when the lateral speed becomes much larger than the pulling speed, the lateral diffusion length D_L/v_y becomes comparable to the radii of curvature close to the trijunction point. In free growth, such conditions are reached only at very large solidification speeds. Under these circumstances, it is clear that the phase-field model no longer reflects quantitatively the sharp-interface equations, since it contains corrective terms due to the finite width of the interface. For instance, we observed a violation of Young's condition at the trijunction point. More precisely, the angles between the interfaces, obtained by taking the tangent vectors to the $\phi=0$ and $\psi=0$ level curves at the trijunction, are still consistent with local equilibrium, but the solid-solid interface is highly curved on a length scale comparable to the width W of the diffuse interface. This is due to the fact that the diffusivity varies smoothly within the diffuse interface, and hence the part of the solid-solid interface near to the trijunction is still able to move. As a result, the angles between the interfaces, seen on a macroscopic scale, differ from the local equilibrium angles. For the purpose of the present study, where we are mainly interested in the qualitative features of the microstructures, we did not investigate this effect quantitatively. Let us remark, however, that such effects may not be simply an artifact of the phase-field model, but may have a physical significance for high growth speeds if the relaxation of the trijunction toward local equilibrium occurs on a time scale comparable to the time of diffusion through the trijunction region.

B. Morphology transition

The results of the preceding section were obtained for systems with lateral extensions of several times the diffusion length. For some sets of parameters, a surprising event occurs when the system size is reduced while all other parameters are kept constant. After some time, the spreading slows down, and the trijunction point may even turn around, such that v_y becomes negative. As a result, the trijunction travels back to the wall where it originated, and an isolated island of β phase, or partial band, is formed. It hence appears that complete spreading is easier to achieve in larger systems, a quite counterintuitive result. Figures 8(a) and 8(b) show time series of typical snapshot pictures for the formation of an island and a band, respectively. The scales are the same on both axes and in both figures. Isoconcentration lines in the liquid are also shown. It can be seen that a lateral concentration gradient builds up in the liquid. This concentration gradient plays an important role in the interpretation of the morphological transition from islands to bands and will be discussed below.

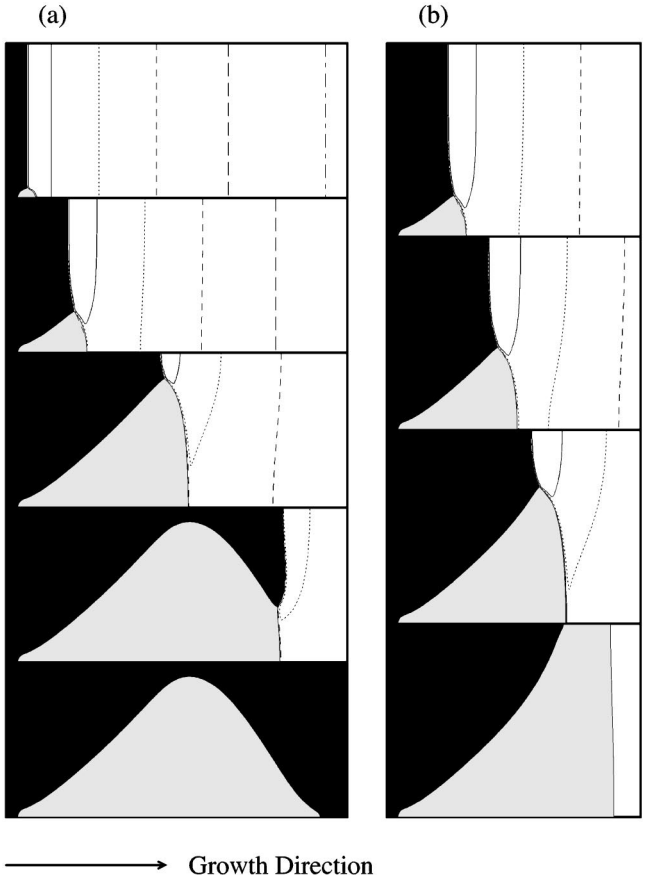

FIG. 8. Spreading of a single β nucleus over the α phase with $\Delta\tilde{T}_N^\beta=0.025\,04, \eta_\beta=0.3125$. (a) Island formation at $L/l_D=0.512$; (b) band formation at $L/l_D=0.64$. Time increases from top to bottom. (Dark region, α phase; light region, β phase; unshaded region, liquid. The isoconcentration lines in the liquid are evenly spaced in c.)

To study more systematically the conditions for the formation of islands, we performed simulations with various lateral system sizes L and compositions c_∞, with the following results.

(1) At a fixed ΔT_N^β, there exists a critical composition c^* such that if $c_\infty<c^*$ the β phase always forms islands. This critical composition decreases as the nucleation undercooling increases.

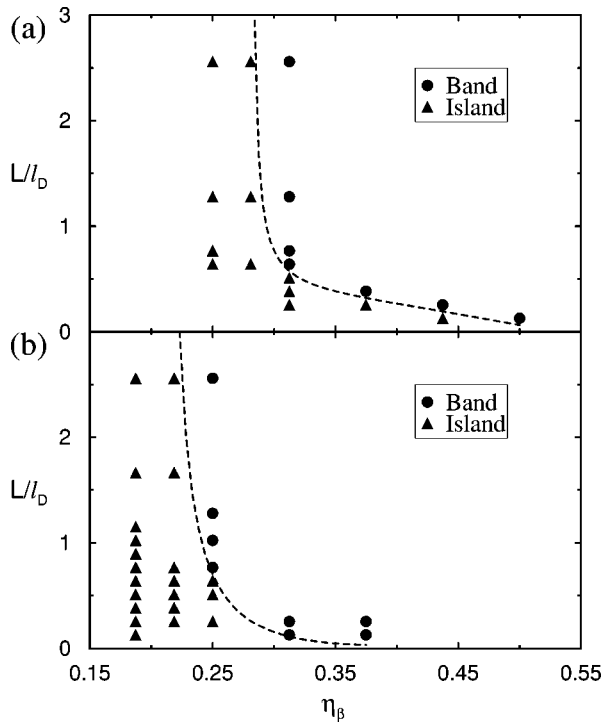

FIG. 9. Morphology map at (a) $\Delta\tilde{T}_N^\beta = 0.025\,04$ and (b) $\Delta\tilde{T}_N^\beta = 0.031\,29$.

(2) At a fixed ΔT_N^β and if $c_\infty > c^*$, there exists a critical lateral system size $L_c(c_\infty)$ such that if the lateral system size $L > L_c$ the β phase spreads completely and forms bands, whereas for $L < L_c$ it forms islands. L_c decreases when either c_∞ or ΔT_N^β increases.

(3) When $c_\infty < c^*$, such that the β phase always forms islands, the final shape (and also the size) of the islands is independent of L when L is larger than a certain size.

Figure 9 shows the final morphology of the system for different c_∞ (or equivalently different η_β) and for different nucleation undercoolings. The dashed lines in Figs. 9(a) and 9(b) represent an estimate for the critical system size $L_c(c_\infty)$ for the transition from bands to islands. It can be seen that both L_c and c^* are smaller for higher $\Delta\tilde{T}_N^\beta$.

The existence of the critical size L_c can be understood by noticing that both α and β phases have to reject impurities in order to grow, but the concentration jump at the α-liquid interface is larger than that at the β-liquid interface. Since β is the stable phase below T_p, there exists a driving force for the β phase to spread. On the other hand, as β rejects fewer impurities than α, the impurity concentration in front of the β phase rapidly decreases after the nucleation. This creates a lateral concentration gradient and hence an impurity flow from the α to the β side as can be clearly seen in Fig. 8. This lateral impurity backflow will accelerate the growth of α and slow down the growth of β and hence there is a competition between the two phases.

To be more precise, we can consider the following scaling argument. Let us assume for simplicity a constant spreading speed v_s for the β phase. Then the time required by the β phase to spread across the system is L/v_s. On the other hand, impurities diffuse laterally through the system on a time scale of L^2/D_L. If $L/v_s < L^2/D_L$, the β phase is able to spread over the α phase before a significant impurity backflow can occur. If the opposite is true, the impurities have enough time to diffuse and the growth of the β phase is slowed down. Hence, the critical system size is given by

$$L_c \sim \frac{D_L}{v_s}. \tag{42}$$

Another way to interpret the above criterion is to note that the ''diffusion speed,'' which is roughly the speed of the impurities diffusing laterally through the system, is given by D_L/L. If the diffusion speed is smaller than v_s, spreading occurs, and Eq. (42) follows immediately.

Clearly, the above argument is only qualitative. We have assumed a constant lateral spreading speed in Eq. (42), although Fig. 6 shows that the spreading speed varies with time, and hence we can give no explicit expression for v_s as a function of composition and nucleation undercooling. However, we can see from Fig. 6 that, for any given time, the instantaneous spreading speed increases with increasing nucleation undercooling and increasing volume fraction of β phase. This observation, together with Eq. (42), allows us to understand qualitatively the shape of the curves $L_c(c_\infty)$ in Fig. 9. In addition, this criterion allows understanding of the striking finding than spreading is easier in large systems that in small ones.

C. Banding and island formation

So far, we have concentrated on how a single β nucleus spreads on the α phase. It is natural to ask what happens if renucleation is allowed. This is a complicated problem since nucleation is an inherently stochastic phenomenon, which cannot be consistently treated within our deterministic model. However, we can try to gain some insight by incorporating nucleation phenomenologically. We will proceed in two steps. First, we treat repeated nucleation in small samples by deterministic rules to make contact with the recent experiments in the Sn-Cd alloy system [13]. Then, in the next section, we investigate the influence of multiple stochastic nucleations on the pattern formation dynamics in large systems.

For solidification in small systems, it can be assumed that nucleation occurs predominantly at the container walls close to the solid-liquid interface. The density of nuclei and the nucleation rate are very rapidly varying functions of the composition. Therefore, it seems reasonable to assume that a nucleus will form as soon as the concentration in the liquid exceeds the threshold corresponding to the nucleation undercooling. Accordingly, we incorporate repeated nucleation by the following rules (the nucleation of α is handled like the nucleation of β before, by placing a small circular nucleus at the solid-liquid interface).

(1) A nucleus of the new phase is placed at one side of the container as soon as the undercooling of the interface exceeds the nucleation undercooling. If both sides of the box

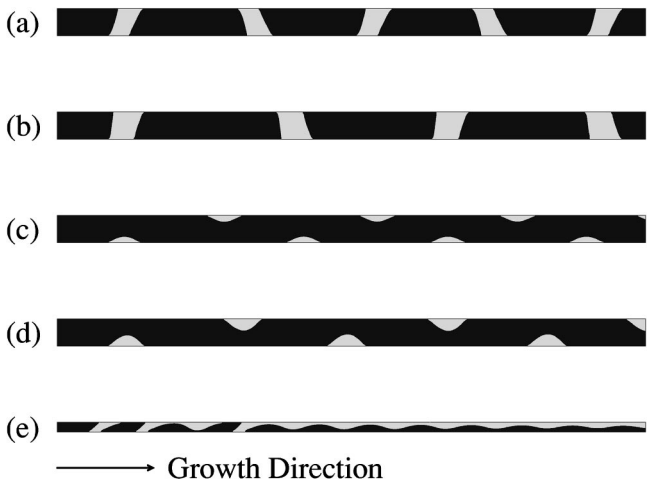

FIG. 10. Microstructures obtained from simulation for (a) $\Delta\tilde{T}_N^{\alpha}=0.135\,65$, $\Delta\tilde{T}_N^{\beta}=0.043\,81$, $L/l_D=0.512$, $\eta_\beta=0.125$, (b) $\Delta\tilde{T}_N^{\alpha}=0.174\,40$, $\Delta\tilde{T}_N^{\beta}=0.056\,33$, $L/l_D=0.512$, $\eta_\beta=0.125$, (c) $\Delta\tilde{T}_N^{\beta}=0.025\,04$, $L/l_D=0.512$, $\eta_\beta=0.05$, (d) $\Delta\tilde{T}_N^{\beta}=0.031\,29$, $L/l_D=0.512$, $\eta_\beta=0.075$ and (e) $\Delta\tilde{T}_N^{\alpha}=0.019\,38$, $\Delta\tilde{T}_N^{\beta}=0.031\,29$, $L/l_D=0.128$, $\eta_\beta=0.4375$. (Dark region, α phase; light region, β phase.)

reach the threshold at the same time, one side is chosen at random.

(2) Once a germ has nucleated, further nucleation of the same phase is prohibited until the germ has either completely spread across the system or completed the formation of an island.

We consider now the two nucleation undercoolings as free parameters, and study different cases. When both ΔT_N^{α} and ΔT_N^{β} are large enough such that the newly nucleated phase spreads completely before the original phase is able to renucleate again, banded structures are obtained. For a smaller ΔT_N^{β}, the β phase does not spread completely, but forms an island. The α phase overtakes the β phase and continues to grow until the nucleation threshold for β is reached again. The islands of β phase form alternately on each side. This is a result of the history of the system: as a result of the formation of the previous island, the concentration of impurities is lower on the side where the last island occurred, and hence nucleation of β is favored at the other side. Examples of these banded and island structures are shown in Fig. 10(a) to Fig. 10(d). The scales on both axes in these figures are the same, but Fig. 10(e) has a different scale from Figs. 10(a)–(d). This last picture was obtained by a simulation at much smaller ΔT_N^{α}, and the lateral size of the system is smaller. In this case, an oscillatory structure is obtained which tends to approach a coupled growth steady state after a complicated transient.

These results are in good qualitative agreement with microstructures obtained in small samples of Sn-Cd alloy [13]. In the experiments, islands tend to form always on the same side of the sample. We believe that this is due to a slight lateral temperature gradient across the sample, which is always present in experiments.

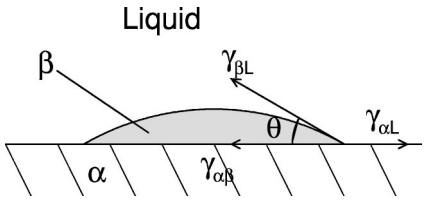

FIG. 11. Sketch of a critical nucleus in the spherical cap model for heterogeneous nucleation.

D. Nucleation controlled microstructures in spatially extended systems

Until now, we have mainly focused on the microstructures formed in small samples. It is interesting to ask what kinds of structure are to be expected in large samples in the absence of convection. This situation could be achieved either in quasi-two-dimensional thin samples, or in a microgravity environment. To model the microstructure formation, larger scale computations were carried out. However, in a spatially extended system, multiple nucleations are unavoidable and must be incorporated in a way that is consistent with the predictions of classical nucleation theory. We chose to extend our model by incorporating the effects of multiple nucleation in a phenomenological manner.

For the nucleation of the β phase on a planar α front (the same arguments also apply to the nucleation of α on β), classical nucleation theory predicts the nucleation rate

$$I=I_0\, e^{-\Delta F^*/k_BT}, \tag{43}$$

where I_0 is a constant prefactor (with dimension equal to the number of nucleations per unit volume per unit time) and ΔF^* is the activation energy for heterogeneous nucleation. Assuming that the critical nucleus is a spherical cap on a planar substrate (the spherical cap model), ΔF^* is given, respectively, in two and three dimensions by

$$\Delta F^*=\begin{cases}\dfrac{\gamma_{\beta L}^2}{\Delta F_B}\times\dfrac{\theta^2}{\theta-(1/2)\sin 2\theta}, & \text{2D}\\[2ex] \dfrac{\gamma_{\beta L}^3}{\Delta F_B^2}\times\dfrac{16\pi(2+\cos\theta)(1-\cos\theta)^2}{12}, & \text{3D,}\end{cases} \tag{44}$$

where ΔF_B is the difference between the bulk free energy of the β phase and of the liquid phase. The contact angle θ, as shown schematically in Fig. 11, is determined by the balance of surface tensions parallel to the substrate,

$$\gamma_{\alpha L}=\gamma_{\alpha\beta}+\gamma_{\beta L}\cos\theta. \tag{45}$$

Assuming that the system is locally in thermodynamic equilibrium, it can be shown that ΔF_B is proportional to $(T-T_p)$ [26], such that for a quasi-two-dimensional system the nucleation rate for β on α can be written as

$$I=\begin{cases}I_{2D}\exp[-A/(T-T_p)^2] & \text{if } T<T_p\\ 0 & \text{if } T\geqslant T_p,\end{cases} \tag{46}$$

where A is a constant, and I_{2D} has now the dimension of number of nucleations per unit time and per unit length of the interface. A similar expression with $w=0$ when $T \leqslant T_p$ holds for α nucleating on β. The 3D form of ΔF^* is used in deriving Eq. (46) since, in practice, the size of a nucleus is still much smaller than the thickness of a thin sample. Equation (46) determines the local nucleation rate and hence the probability per unit time of a nucleus forming as a function of the local temperature at the solid-liquid interface.

Unfortunately, both experimental and theoretical estimates of the free energy barrier and the kinetic prefactor are scarce in the context of heterogeneous nucleation, since the actual values may depend on complicated details of the interfacial structure. Since, in the present study, we focus on morphological aspects of the large scale structure, we decided to treat the two quantities as free parameters. Moreover, we want to compare the stochastic simulations to the deterministic runs of the preceding sections. Consequently, we may eliminate one of those two parameters by the requirement of recovering the rules used previously. That is, in the deterministic simulations a nucleus was put at the solid-liquid interface when it reached the predetermined nucleation undercooling. In the stochastic runs, nucleation should therefore occur with probability 1 for the same interface temperature. This condition will lead to a relation between the prefactor and the energy barrier in the nucleation rate.

To proceed, let us first specify how we treat nucleation in the simulation algorithm. The interface is scanned at a regular time interval Δt_N, and nucleation is attempted at points regularly spaced by a distance Δs_N along the interface. The nucleation rate may be rewritten as

$$I = \frac{w(T)}{\Delta t_N \Delta s_N}, \tag{47}$$

where

$$w = \begin{cases} w_0 \exp[-A/(T-T_p)^2] & \text{if } T < T_p \\ 0 \quad \text{if } T \geqslant T_p \end{cases} \tag{48}$$

is a dimensionless function of the interface temperature. At each test point, a nucleus is generated with probability 1 if $w>1$, and with probability w otherwise. That is, if $w<1$, a random number ξ uniformly distributed between 0 and 1 is drawn, and a nucleus is generated if $\xi<w$. As before, the nucleus is spherical and has a size of $6W$. A possible drawback of the procedure outlined above is that the actual nucleation rate depends on the values chosen for Δt_N and Δs_N. However, it is reasonable to assume that the microstructures should not depend too sensitively on the choice of these parameters as long as their values are much smaller than the time and length scales of the pattern formation process.

Now we can relate the prefactor and the barrier in the nucleation rate. In the preceding sections, nuclei were introduced deterministically when the nucleation undercooling was reached, that is, at a nucleation temperature

$$T_N^\beta = T_p - \frac{\Delta T_N^\beta}{1 - m_\beta / m_\alpha}. \tag{49}$$

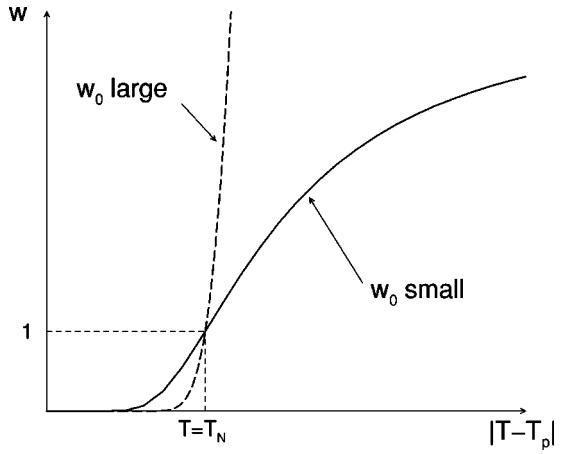

FIG. 12. Schematic plot of the dimensionless nucleation rate $w(T)$ versus temperature for two different choices of w_0 and A.

This implies that in the stochastic algorithm we must choose

$$w(T_N^\beta) = w_0 \exp[-A/(T_N^\beta - T_p)^2] = 1. \tag{50}$$

Given this condition, there is only one remaining free parameter; we choose the dimensionless kinetic prefactor w_0. This parameter controls the temperature range over which nucleations occur. Indeed, $w(T)$ is a function that rapidly increases in a narrow temperature range around T_N^β. Increasing w_0 and A simultaneously while respecting the constraint Eq. (50), the rise of the nucleation rates becomes sharper, as shown schematically in Fig. 12.

Now consider an α-liquid interface during its transient, when the temperature at the interface is decreasing from above T_p to its steady-state temperature. If the temperature range over which the nucleation rate increases significantly is narrow, all nucleation events will occur almost at the same time when the interfacial temperature coincides with T_N^β. As a result, the mean separation between the nuclei will be small. On the other hand, if w_0 is small, nuclei appear with a broader spread in interfacial temperature, and the mean separation between the nuclei will be larger. Since the mean separation between the nuclei plays a similar role as the system size in a small sample experiment, we might expect a morphology transition from bands to islands as w_0 is increased.

Figure 13 shows the microstructures obtained in simulations for small w_0, ranging from 5×10^3 to 5×10^5. The lateral system size is about twice the diffusion length, and we use periodic boundary conditions in the direction perpendicular to the temperature gradient. The lateral spreading of multiple nuclei leads to a jagged morphology. Each V-shaped site in the figures indicates a nucleation event (either β on α or α on β). A transition from irregular banded structures to islands can be observed as w_0 increases. Note, however, that nucleation events occur in bursts, leading to a spatial periodicity along the growth direction that can be clearly distinguished in Fig. 13(c). This means that there is still a ''banding cycle,'' now consisting of layers of a two-phase composite structure (*particulate* structure) and layers of pure α matrix.

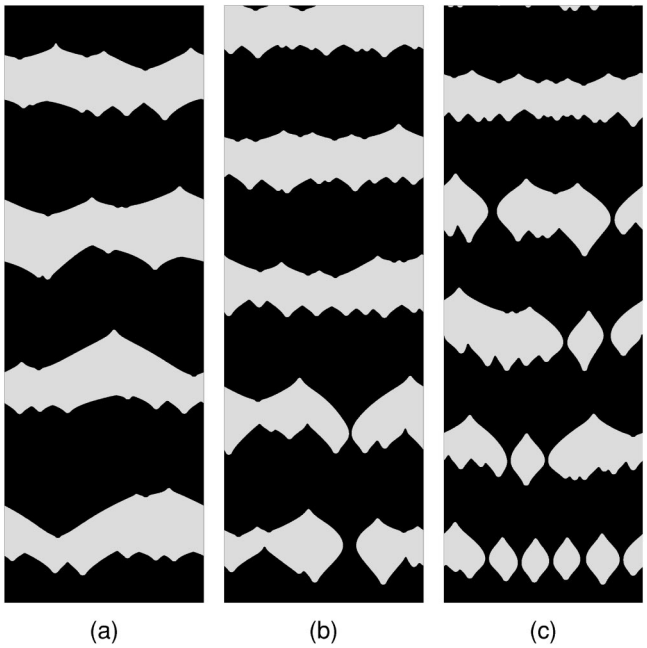

FIG. 13. Microstructures obtained from simulations with stochastic nucleation events for $L/l_D=2.048$, $\eta_\beta=0.25$, $\Delta\tilde{T}_N^\alpha=\Delta\tilde{T}_N^\beta=0.031\,29$, and (a) $w_0=5\times10^3$, (b) $w_0=5\times10^4$, (c) $w_0=5\times10^5$. Growth is from bottom to top; dark regions, α phase; light regions, β phase.

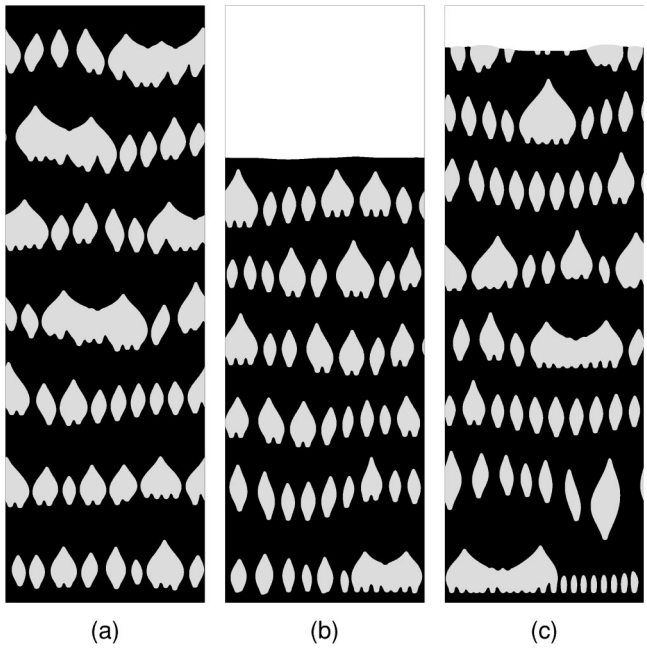

FIG. 14. Microstructures obtained from simulations with stochastic nucleation events: (a) $w_0=5\times10^{11}$, (b) $w_0=5\times10^{26}$, (c) $w_0=5\times10^{43}$; other parameters as in Fig. 13. The unshaded region is the liquid.

The values for w_0 in Fig. 13 are somewhat small. The attempt rate w_0 should be related to the rate I_0 in Eq. (43), which is typically about 10^{30} nuclei/cm^3 s for heterogeneous nucleation in metallic systems [11]. Hence we investigated the microstructures formed with larger values of w_0, ranging from 5×10^{11} to 5×10^{43}. In this range, we always obtain island structures that look qualitatively similar (Fig. 14), and not too different from Fig. 13(c). This implies that the microstructures obtained with multiple nucleation events are not very sensitive to w_0 when w_0 is larger than some critical value. Hence we would expect predominantly island structures in spatially extended systems.

The last statement, however, is valid only for the quite restrictive assumptions made in our model. Most importantly, we have assumed that the probability of nucleation depends only on the composition in the liquid, and not on the local geometry of the interface. This neglects the presence of grain boundaries and impurities (bubbles, inclusions) which can considerably enhance nucleation. Such heterogeneities broaden the distribution of the nucleation rate as a function of temperature, and would hence favor bands. The evolution of the grain structure could in principle be modeled by including the local crystalline orientation as an additional order parameter. An interesting perspective is that the interplay between nucleation at grain boundaries and spreading might select a certain grain size, since for small grains a spreading phase can engulf and hence ''heal'' grain boundaries, whereas for large grains nucleation at the solid-liquid interface (as modeled in our simulations) may occur and lead to the formation of new grains. Such a study, however, is largely beyond the scope of this article.

VI. SUMMARY AND CONCLUSIONS

We have developed a phase-field model to investigate a class of banded microstructures that form during the directional solidification of peritectic alloys under purely diffusive growth conditions. We focused on a regime of large thermal gradients and low pulling speeds where both phases are morphologically stable and the interface dynamics is controlled by a subtle interplay between the growth and nucleation of two competing solid phases, rather than by the morphological instability of one phase. We restricted our attention to a generic peritectic phase diagram that simplified both the models and the computations, but our approach is in principle flexible enough to be extended to phase diagrams of specific materials.

The two-dimensional simulations of this model have shed light on three main aspects of banding: the transition from islands to bands that has been observed in narrow samples where convection is suppressed [13], the associated dynamical spreading of one phase onto the other, and the type of structures that one would expect to form in wide samples under purely diffusive growth conditions that are not presently accessible in an earth-based laboratory, at least for the alloys investigated to date.

We have shown that the transition from islands to bands can be understood in terms of a competition between the lateral spreading of β on α and the diffusive backflow of rejected impurities from α to β. This competition leads to the surprising result that bands tend to form more easily in wider samples, in qualitative agreement with recent experiments in the Sn-Cd alloy carried out in small samples in order to suppress convection [13]. The critical system size L_c at which this transition occurs depends on the nucleation

undercooling for the β phase that influences the spreading rate, and on the alloy composition, with L_c becoming infinite when the volume fraction of the β phase falls below a minimum value necessary for band formation. The influence of other parameters, in particular the form of the phase diagram and the equilibrium angles at the trijunction, has not been investigated in detail here.

When the peritectic phase fully covers the parent phase, its spreading dynamics is characterized by a remarkably uniform acceleration of the moving trijunction that depends on the composition, but not on the nucleation undercooling. This acceleration originates from an increase with time of the local supersaturation (driving force for spreading) associated with the relaxation of the planar parent phase ahead of the trijunction to its steady state below T_p, together with a direct relationship between the instantaneous speed of the trijunction and this driving force that depends on the material properties, but not on the history or the overall composition of the sample. Moreover, the relative angles between phase boundaries at the trijunction during rapid spreading depart significantly from those prescribed by Young's condition, indicating a strong departure from local equilibrium. Both predictions might be experimentally testable in transparent organic eutectic systems that exhibit similar spreading transients before coupled growth is established [27].

The formation of multiple nuclei in wide samples ($L \gg L_c$) adds a stochastic element to the interface dynamics that renders the range of possible patterns even richer. One can nonetheless distinguish two basic types of structure that can be understood within the framework of the single island to band transition in narrow samples ($L \sim L_c$). The first is a discrete banded structure made up of separate jagged bands that span the whole width of the sample. The second is a *particulate* banded structure made up of approximate rows of particles (islands) of the peritectic phase embedded in the matrix of the parent phase. The banded (particulate) structure is naturally selected if the mean distance between nuclei is larger (smaller) than the critical sample width L_c for the island-band transition, and, moreover, simulations reveal that the particulate structure is preferred if nucleation is assumed to follow a classical nucleation law. Even though we modeled patterns in wide samples with such a law, we expect the transition from a discrete to a particulate banded structure to be generally governed by the mean distance between nuclei even if other nucleation mechanisms (such as wall-induced nucleation and nucleations at grain boundaries) play a dominant role. Both types of structure could conceivably coexist in the same sample if nucleation conditions change during growth.

There are a number of possible extensions of the present study. One is to investigate the patterns that form for a somewhat larger range of pulling speeds where the parent phase is morphologically unstable, but the peritectic phase is still linearly stable. Another is to incorporate the influence of convection in a fully consistent way to make contact with experiments over a wider range of sample sizes, which is now possible within a phase-field context [28,29].

ACKNOWLEDGMENTS

This research has been supported by the NASA Microgravity Research Program under Grant No. NAG8-1254 and by U.S. DOE Grant No. DE-FG02-92ER45471. Computations were made possible by the allocation of time at the Northeastern University Advanced Scientific Computation Center (NUASCC). We thank J. S. Park, R. Trivedi, S. Akamatsu, and G. Faivre for many helpful discussions and for giving us access to their experimental results prior to publication.

APPENDIX: RESULTS OF THE COMMON TANGENT CONSTRUCTION

The common tangent construction allows one to determine the equilibrium composition for two-phase equilibrium for given bulk free energies f_ν of the two phases. For two-phase equilibrium, the bulk phases must have equal chemical potentials $\mu = df_\nu/dc$ and grand potentials $\Omega = f_\nu - \mu c$. Solving the resulting equations for our model bulk free energies, we find for solid-liquid equilibrium

$$c_L^{\alpha,\beta} = \frac{\left(B_1 \pm \frac{1}{2}B_2\right)}{\left(A_1 \pm \frac{1}{2}A_2\right)} + A_1, \tag{A1}$$

$$c_S^{\alpha,\beta} = \frac{\left(B_1 \pm \frac{1}{2}B_2\right)}{\left(A_1 \pm \frac{1}{2}A_2\right)} - A_1 \mp A_2. \tag{A2}$$

The upper (lower) sign is for the α (β) phase.

For solid-solid equilibrium, we get

$$c_{SS}^{\alpha} = \frac{B_2}{A_2} - A_1 - A_2, \tag{A3}$$

$$c_{SS}^{\beta} = \frac{B_2}{A_2} - A_1 + A_2. \tag{A4}$$

For convenience, we define

$$\overline{A} = (A_1 \pm \tfrac{1}{2}A_2) \tag{A5}$$

and

$$\overline{B} = (B_1 \pm \tfrac{1}{2}B_2) \tag{A6}$$

where the upper (lower) sign is for the α (β) phase.

In order to relate the parameters in our model to a physical system, let us write

$$B_1 = B_{11} + B_{12}\tilde{T}, \tag{A7}$$

$$B_2 = B_{21} + B_{22}\tilde{T}. \tag{A8}$$

Here, c and $\tilde{T}$ are the scaled composition and temperature, respectively, defined in the text. Let ΔC_ν and m_ν be the concentration jump at the solid-liquid interface and the liquidus slope of phase ν, respectively, at T_p. Let r be the ratio $\Delta C_\beta/\Delta C_\alpha$; then the parameters A_1, A_2, B_{11}, B_{12}, B_{21}, and B_{22} are related to these quantities in the phase diagram by

$$A_1=\frac{1}{4}(1+r), \tag{A9}$$

$$A_2=\frac{1}{2}(1-r), \tag{A10}$$

$$B_{11}=\frac{1}{4}(1+r)\left[r-\frac{1}{4}(1+r)\right], \tag{A11}$$

$$B_{21}=\frac{1}{2}(1-r)\left[r-\frac{1}{4}(1+r)\right], \tag{A12}$$

$$B_{12}=-\frac{1}{4}\left(1+r\frac{m_\alpha}{m_\beta}\right), \tag{A13}$$

$$B_{22}=-\frac{1}{2}\left(1-r\frac{m_\alpha}{m_\beta}\right). \tag{A14}$$

In order to have vertical solid-solid coexistence lines, we have to choose the parameters such as to make B_{22} vanish. The parameters for our model peritectic system are listed in Table II.

TABLE II. Parameters for our model peritectic system.

C_p	38.2 wt %	A_1	3.30745×10^{-1}
$C_{p\alpha}$	22.1 wt %	A_2	3.38509×10^{-1}
$C_{p\beta}$	33.0 wt %	B_{11}	-2.56790×10^{-3}
m_α	−6.71865 K/wt %	B_{21}	-2.62818×10^{-3}
m_β	−2.17 K/wt %	B_{12}	−0.5
		B_{22}	0.0

[1] W. J. Boettinger, S. R. Coriell, A. L. Greer, A. Karma, W. Kurz, M. Rappaz, and R. Trivedi, Acta Mater. **48**, 43 (2000).

[2] W. W. Mullins and R. F. Sekerka, J. Appl. Phys. **3**, 444 (1964).

[3] T. Umeda, T. Okane, and W. Kurz, Acta Mater. **44**, 4209 (1996).

[4] W. J. Boettinger, Metall. Trans. **5**, 2023 (1974).

[5] H. D. Brody and S. A. David, in *Proceedings of the International Conference on Solidification and Casting* (Institute of Metals, London, 1977), Vol. 1, p. 144.

[6] A. P. Titchener and J. A. Spittle, Acta Metall. **23**, 497 (1975).

[7] A. Ostrowski and E. W. Langer in *Proceedings of the International Conference on Solidification and Casting* (Ref. [5]), p. 139.

[8] N. J. W. Barker and A. Hellawell, Met. Sci. **8**, 353 (1974).

[9] B. C. Fuh, Ph.D thesis, Iowa State University, Ames, IA, 1984.

[10] M. Vandyoussefi, H. W. Kerr, and W. Kurz, Acta Mater. **45**, 4093 (1997); M. Vandyoussefi, Ph.D. thesis, École Polytechnique Fédérale de Lausanne, Switzerland, 1997.

[11] R. Trivedi, Metall. Mater. Trans. A **26A**, 1 (1995).

[12] A. Karma, W. J. Rappel, B. C. Fuh, and R. Trivedi, Metall. Mater. Trans. A **29A**, 1457 (1998).

[13] J. S. Park and R. Trivedi, J. Cryst. Growth **187**, 511 (1998); R. Trivedi *et al.*, *Proceedings of the 1998 Zermatt Workshop on Solidification Microstructures*, edited by M. Pappaz and R. Trivedi. (This CD may be obtained from the laboratory of physical metallurgy, EPFL, Lausanne, Switzerland.)

[14] P. Mazumder, R. Trivedi, and A. Karma, in *Phase Transformations and Systems Driven Far From Equilibrium*, edited by E. Ma *et al.*, MRS Symposia Proceedings Vol. 481 (Materials Research Society, Pittsburgh, 1998), pp. 39–44.

[15] J. S. Langer, in *Directions in Condensed Matter Physics*, edited by G. Grinstein and G. Mazenko (World Scientific, Singapore, 1986), pp. 164–186.

[16] A. A. Wheeler, W. J. Boettinger, and G. B. McFadden, Phys. Rev. A **45**, 7424 (1992).

[17] J. A. Warren and W. J. Boettinger, Acta Metall. Mater. **43**, 689 (1995).

[18] A. Karma and W.-J. Rappel, Phys. Rev. E **57**, 4323 (1998).

[19] W. Losert, D. A. Stillman, H. Z. Cummins, P. Kopczyński, W.-J. Rappel, and A. Karma, Phys. Rev. E **58**, 7492 (1998).

[20] A. Karma, Phys. Rev. E **49**, 2245 (1994).

[21] K. R. Elder, F. Drolet, J. M. Kosterlitz, and M. Grant, Phys. Rev. Lett. **72**, 677 (1994).

[22] A. A. Wheeler, G. B. McFadden, and W. J. Boettinger, Proc. R. Soc. London, Ser. A **452**, 495 (1996).

[23] J. Tiaden, B. Nestler, H. J. Diepers, and I. Steinbach, Physica D **115**, 73 (1998).

[24] T. S. Lo, Ph.D. thesis, Northeastern University, Boston, 1999.

[25] J. A. Warren and J. S. Langer, Phys. Rev. E **47**, 2702 (1993).

[26] J. W. Christian, *The Theory of Transformations in Metals and Alloys*, 1st ed. (Pergamon Press, Oxford, 1965), p. 537.

[27] G. Faivre and S. Akamatsu (unpublished).

[28] C. Beckermann, H.-J. Diepers, I. Steinbach, A. Karma, and X. Tong, J. Comput. Phys. **154**, 468 (1999).

[29] X. Tong, C. Beckermann, and A. Karma, Phys. Rev. E **61**, R49 (2000).